A final version of this paper was published in
IEEE Trans. Vehicular Technology 70 (2021), pp. 3197-3207, DOI 10.1109/TVT.2021.3065924

A Linear Eddy Current Speed Sensor with a Perpendicular Coils Configuration

Mehran Mirzaei and Pavel Ripka

***Abstract*—This paper presents a new linear eddy current speed sensor with rectangular-shaped coils. The excitation coil and the pick-up coil have a perpendicular configuration without a magnetic yoke. The proposed sensor is shorter than the previous designs. The sensor works for a conductive moving target; in this paper we present calculations and an experimental verification for solid iron and aluminum moving part materials. A novel 3D analytical method is presented for the description and for the design of an eddy current speed sensor that is fast and has high precision. The source fields and the reaction fields caused by induced eddy currents are separated in our 3D analytical method, which facilitates an enhanced investigation of the features of the speed sensor. Evaluations of the effects of the moving part material and of coil lift off on the performance of the speed sensor are made with the use of a 3D analytical method. Measurements are performed for an eddy current speed sensor at different speeds up to 11.65 m/s and at different frequencies with a novel analytical model in terms of the induced voltage in the pickup coil versus speed. Simplicity and high precision are the main advantages of the proposed speed sensor. The achieved linearity error is 0.47% (measured) up to 11.6 m/s, and 0.43% (calculated) up to 117 m/s (420 km/h).**

***Index Terms*—Eddy current, speed sensor, perpendicular coils, 3D analytical method, conductive targets**

I. Introduction

SPEED measurements of moving objects are essential for industry, for example, in railway transportation, trains, metros and Maglev [1]-[3]. Optical sensors and variable reluctance magnetic sensors are widely used for railway speed measurements [4]-[7]. However, they require optical or magnetic saliency on the moving object, and optical sensors are very sensitive to dirt and dust. Other methods are tachometers, microwave Doppler radar, accelerometers, GPS and correlation methods using two sensors for speed measurements in railway applications. Doppler radar is subject to angular error [8], while GPS is not available in tunnels.

Contactless magnetic speed sensors are more suitable for railway applications where there is a high probability of dirt and dust. Existing magnetic speed sensors based on variable reluctance use permanent magnets for excitation or Hall sensors for signal pick-up. However, existing sensors suffer greatly from temperature dependency, especially in a high-temperature environment [9]-[11]. Traditional speed sensors for trains, based on variable reluctance, optical and tachometer measurements, make indirect linear speed measurements, and they are operated on a rotating train wheel [4]. Therefore, any fault in the wheel can cause an error in the speed sensor output. Wheel wear, sliding and slipping are sources of errors in indirect linear speed sensors. A sensorless speed estimation method is also utilized in the linear and rotating propulsion system [12]-[14], but it is insufficiently tolerant to electrical faults in the drive system, and it is also a slower method for speed estimation.

Induced eddy currents have been utilized for a long time in electromagnetic devices for drive, for braking and for measurements such as rotating and linear induction machines, eddy current brakes and eddy current position sensors [15]-[17]. Utilizing the speed component of the induced voltage has a long history in electrical engineering, e.g. the Faraday generator, the homopolar generator, and magnetic flowmeters [18]-[19]. The metal industries also use and evaluate the speed component of induced eddy currents for non-destructive testing [20]-[23].

One type of speed sensor based on eddy currents in a metallic moving body with a smooth surface used a Hall sensor with a two-pole permanent magnet excitation field [24]. The disadvantage of this DC method is the high temperature offset drift caused by the Hall sensor, and the large influence of external magnetic fields. A speed sensor based on the high sensitivity of an amorphous core with a ring shape mounted on a solid iron E shape core for magnetic field excitation was presented in [25]. The contactless eddy current speed sensor for a railway wheel using a freely-rotating permanent magnet rotor presented in [26] in fact measures only the wheel speed and not the rail speed, not the linear speed of the train.

The performance of a parallel (longitudinal) and perpendicular (transversal) eddy current speed sensor with air coils excitation and pick-up air coils was analyzed and measured in [27]-[28]. The moving part in the eddy current speed sensor was made of aluminum, which is a non-magnetic material and has fewer industrial applications than solid irons and steels. The authors have presented linear axisymmetric and longitudinal eddy current speed sensors with air coils and solid iron moving parts [29]-[31], which showed the complexity of the eddy current speed sensor for a solid iron moving part in comparison with aluminum or some other non-magnetic conductive moving part.

The main problem with sensors that use a magnetic core or yoke is poor stability of the sensitivity of the sensor, caused by the changes in magnetic properties with time and temperature. We therefore decided to use air coils, despite their lower sensitivity. A perpendicular-type eddy current speed with air coils is presented in this paper, and measurements are performed up to a maximum speed of 11.65 m/s. An evaluation

A final version of this paper was published in
IEEE Trans. Vehicular Technology 70 (2021), pp. 3197-3207, DOI 10.1109/TVT.2021.3065924

of the performance of the eddy current speed sensor at higher speeds is also presented.

II. Modeling

Fig. 1 shows a 3D computational model of the eddy current sensor. The pick-up coil is perpendicular to the excitation coil. The pick-up coil is located exactly in the middle of the excitation coil. The induced voltage in the pick-up coil is zero when the speed, V, is zero, as the excitation coil magnetic flux is symmetrical and the flux linkage to the pick-up coil is zero. The pick-up coil voltage is not zero at nonzero speed, as the speed of the moving part causes the magnetic flux to be unsymmetrical.

Fig. 2 and Fig. 3 show 2D views of the eddy current speed sensor in the y-x and z-x planes. Table I presents the parameters of the eddy current speed sensor and the moving part parameters and dimensions according to Fig. 2 and Fig. 3. The dimensions and the parameters of the excitation coil and the pick-up coil are constant in this paper. However, the analytical modeling is general for different dimensions and parameters of the excitation and pick-up coils.

TABLE I
Eddy Current Speed Sensor Parameters

Parameter	Definition	Value
N_e=N_p	number of turns in each coil	200
I	current amplitude	0.135 A
L	moving part width	110 mm
d	moving part thickness	5 mm
w_c	inner coil width	40 mm
h_c	height of each coil	5 mm
t_c	thickness of each coil	3.5 mm
g_m	gap between coil and moving part	6.25 mm
g_c	gap between coils	2.5 mm
σ_i	solid iron conductivity	6.0 MS/m
σ_a	solid aluminum conductivity	33.5 MS/m
μ_r	solid iron permeability	100

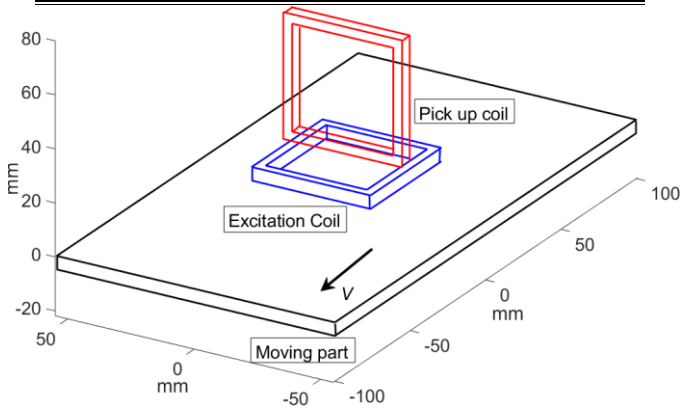

Fig. 1. A 3D computational model of the eddy current speed sensor with perpendicular configuration of the excitation coil and the pick-up coil and the moving part with speed, V

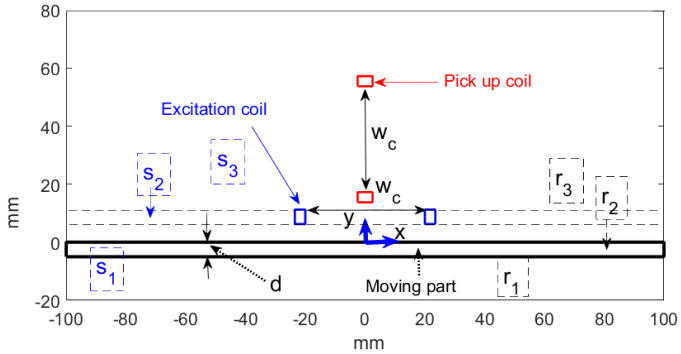

Fig. 2. A 2D view of the eddy current speed sensor in the y-x plane with computation regions, s_1, s_2 and s_3 related to the source fields of the excitation coil, and r_1, r_2 and r_3 related to the reaction fields of the moving part

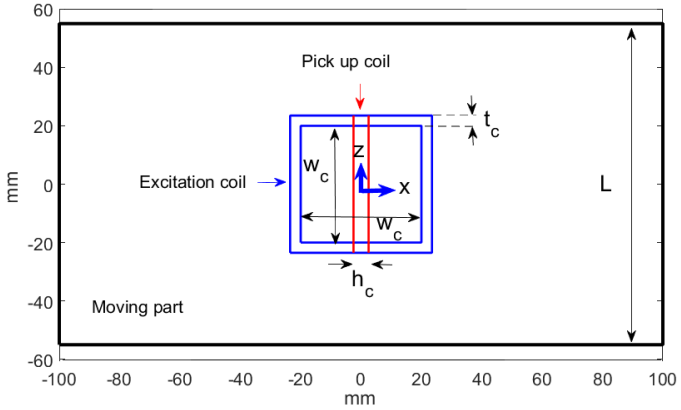

Fig. 3. A 2D view of the eddy current speed sensor in the z-x plane

The magnetic analyses of eddy current speed sensor are presented in two steps to separate source fields of excitation coils and reaction fields of induced eddy current in the moving part. This procedure also simplifies the analytical modeling of the eddy current speed sensor.

A. Only the Excitation Coil

First, only the magnetic fields caused by the excitation coil are considered as a source field. The partial differential equations in 3D utilizing the x and z component of the magnetic vector potential, A_x and A_z, derived from the Maxwell equations, are presented in (1) [32] for three regions s_1, s_2 and s_3 in Fig. 2. Regions s_1, s_2 and s_3 are addressed to the parts in Fig. 2 that are below the excitation coil, the excitation coil, and above the excitation coil, respectively.

$$\begin{aligned}
&\frac{\partial^2 A_{z,s_1}}{\partial x^2}+\frac{\partial^2 A_{z,s_1}}{\partial y^2}+\frac{\partial^2 A_{z,s_1}}{\partial z^2}=0\\
&\frac{\partial^2 A_{z,s_2}}{\partial x^2}+\frac{\partial^2 A_{z,s_2}}{\partial y^2}+\frac{\partial^2 A_{z,s_2}}{\partial z^2}=-\mu_0 J_{s,z}\\
&\frac{\partial^2 A_{z,s_3}}{\partial x^2}+\frac{\partial^2 A_{z,s_3}}{\partial y^2}+\frac{\partial^2 A_{z,s_3}}{\partial z^2}=0
\end{aligned} \tag{1}$$

A magnetic gauge condition is necessary to obtain a unique solution of (1). Coulomb gauge and Lorentz gauge are usually used for gauging [32]-[36]. They give ~~cause~~ the same results in numerous magnetic models with the eddy currents [34].

A final version of this paper was published in
IEEE Trans. Vehicular Technology 70 (2021), pp. 3197-3207, DOI 10.1109/TVT.2021.3065924

However, Coulomb gauge is more suitable in nonconductive regions and it does not include electrical scalar potential in the formulation. Therefore, Coulomb gauge condition in (2) is considered to obtain solutions for A_x and A_z.

$$\nabla \cdot A = 0 \rightarrow \frac{\partial A_x}{\partial x} + \frac{\partial A_z}{\partial z} = 0 \tag{2}$$

Only the x and z component of the magnetic vector potential, A_x and A_z, are considered, as the excitation coil is parallel to the conductive moving part or the z-x plane, and the y component of the magnetic vector potential, A_y, is considered negligible. J_s is the source current density in (1) corresponding to region s_2.

The separation of variables method is used to solve the partial differential equations in (1). Equations (3) and (4) are based on these assumptions that the magnetic fields are a sinusoidal function versus time, $e^{j\omega t}$, and the periodical sinus series functions in x and z directions with $2l$ and $2L$ periods, $e^{-j(k_m x + k_n z)}$, respectively [32], [36]-[37]. Parameters l and L are ~~longitudinal~~ length and ~~transversal~~ width of the model in x-direction and z-direction, respectively. They correspond to the boundaries, where magnetic fields are specified as zero values.

$$A_z = \sum_n \sum_m A_z^{m,n},\ A_z^{m,n} \propto e^{j(\omega t - k_m x - k_n z)} \tag{3}$$

$$\begin{aligned}
&\frac{\partial A_z^{m,n}}{\partial x} = -jk_m A_z^{m,n},\ \frac{\partial^2 A_z^{m,n}}{\partial x^2} = -k_m^2 A_z^{m,n},\\
&k_m = m\frac{\pi}{l}, m = \pm 1, \pm 3, \cdots\\
&\frac{\partial A_z^{m,n}}{\partial z} = -jk_n A_z^{m,n},\ \frac{\partial^2 A_z^{m,n}}{\partial z^2} = -k_n^2 A_z^{m,n},\\
&k_n = n\frac{\pi}{L}, n = \pm 1, \pm 3, \cdots\\
&\frac{\partial A_z}{\partial t} = j\omega \cdot A_z, \quad \omega = 2\pi f
\end{aligned} \tag{4}$$

where, f is frequency. The solutions of (1) are calculated in (5) and (6) for regions s_1, s_2 and s_3.

$$\begin{aligned}
&A_{z,s_1}^{m,n} = \left(C_{1,s_1} e^{\gamma \cdot y} + C_{2,s_1} e^{-\gamma \cdot y}\right) \cdot e^{j(\omega t - k_m x - k_n z)}\\
&\gamma = \sqrt{k_m^2 + k_n^2},\ A_{x,s_1} = -\frac{k_n}{k_m} A_{z,s_1}\\
&A_{z,s_2}^{m,n} = \left(C_{1,s_2} e^{\gamma \cdot y} + C_{2,s_2} e^{-\gamma \cdot y} + \frac{\mu_0 J_p^{m,n}}{\gamma^2}\right) \cdot e^{j(\omega t - k_m x - k_n z)}\\
&A_{x,s_2} = -\frac{k_n}{k_m} A_{z,s_2}\\
&A_{z,s_3}^{m,n} = \left(C_{1,s_3} e^{\gamma \cdot y} + C_{2,s_3} e^{-\gamma \cdot y}\right) \cdot e^{j(\omega t - k_m x - k_n z)}\\
&A_{x,s_3} = -\frac{k_n}{k_m} A_{z,s_3}
\end{aligned} \tag{5}$$

$$\begin{aligned}
&J_p^{m,n} = 2\frac{j}{n\pi l} C_J \cdot J_s, \qquad J_s = \frac{N_e \cdot I}{h_c \cdot t_c}\\
&C_J = \frac{1}{k_m + k_n} C_{J,1} - \frac{1}{k_m - k_n} C_{J,2}\\
&C_{J,1} = \sin\left(k_m \frac{w_c + 2t_c}{2} + k_n \frac{w_c + 2t_c}{2}\right)\\
&-\sin\left(k_m \frac{w_c}{2} + k_n \frac{w_c}{2}\right)\\
&C_{J,2} = \sin\left(k_m \frac{w_c + 2t_c}{2} - k_n \frac{w_c + 2t_c}{2}\right)\\
&-\sin\left(k_m \frac{w_c}{2} - k_n \frac{w_c}{2}\right)
\end{aligned} \tag{6}$$

Parameter J_p in (6) corresponds to the source coil modeling (Fig. 4), which are calculated for rectangular coils with right-angled corners instead of round corners to simplify formula~~tion~~s in (6). Using right-angled corners has negligible error as the round part has relatively small length to the whole length of the coil. The constants C_1's and C_2's in (5) are calculated using boundary conditions between regions s_1, s_2 and s_3 in (7), which are presented in (8). Parameters B_y, H_x and H_z in (7) and (8) are the y-component of the magnetic flux density, the x-component of the magnetic field strength and the z-component of magnetic field strength, respectively.

$$\begin{aligned}
&A_{z,s_1}(y = -\infty) = 0\\
&H_{x,z,s_1}(y = g_m) = H_{x,z,s_2}(y = g_m)\\
&B_{y,s_1}(y = g_m) = B_{y,s_2}(y = g_m)\\
&H_{x,z,s_2}(y = g_m + h_c) = H_{x,z,s_3}(y = g_m + h_c)\\
&B_{y,s_2}(y = g_m + h_c) = B_{y,s_3}(y = g_m + h_c)\\
&A_{z,s_3}(y = \infty) = 0
\end{aligned} \tag{7}$$

$$\begin{aligned}
&H_x = \frac{1}{\mu_0 \mu_r}\frac{\partial A_z}{\partial y},\ B_y = \frac{\partial A_x}{\partial z} - \frac{\partial A_z}{\partial x},\ H_z = -\frac{1}{\mu_0 \mu_r}\frac{\partial A_x}{\partial y}\\
&C_{1,s_1} = \frac{\mu_0 J_p^{m,n}}{\gamma^2} e^{-\gamma \cdot \left(g_m + \frac{h_c}{2}\right)} \sinh\left(\gamma \cdot \frac{h_c}{2}\right),\ C_{2,s_1} = 0\\
&C_{1,s_2} = -\frac{\mu_0 J_p^{m,n}}{2\gamma^2} e^{\gamma \cdot g_m},\ C_{2,s_2} = -\frac{\mu_0 J_p^{m,n}}{2\gamma^2} e^{\gamma \cdot (g_m + h_c)}\\
&C_{1,s_3} = 0,\ C_{2,s_2} = \frac{\mu_0 J_p^{m,n}}{\gamma^2} e^{\gamma \cdot \left(g_m + \frac{h_c}{2}\right)} \sinh\left(\gamma \cdot \frac{h_c}{2}\right)
\end{aligned} \tag{8}$$

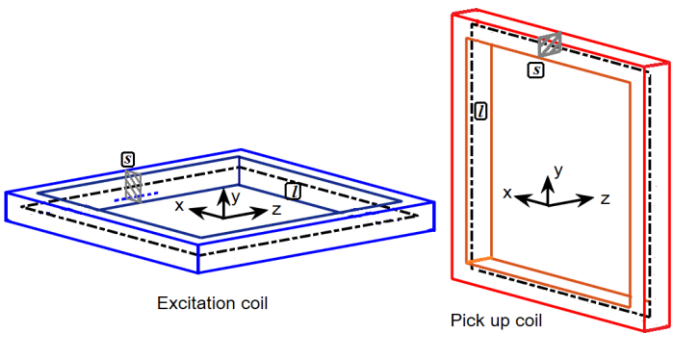

Fig. 4. 3D view of the excitation coil and the pick up coil and integration line, l and integration surface, s of (9), (14) and (15)

A final version of this paper was published in
IEEE Trans. Vehicular Technology 70 (2021), pp. 3197-3207, DOI 10.1109/TVT.2021.3065924

The self-inductance of the excitation coil related only to the excitation coil fields, $L_{e\text{-}s}$ is as follows:

$$L_{e-s}=\frac{\Psi_{e-s}}{I}=\frac{N_e\int\int A_{s_2}\cdot dlds}{h_c\cdot t_c\cdot I}=$$
$$\frac{N_e\cdot L\cdot l}{h_c\cdot t_c\cdot I}\sum_n\sum_m C_{L-s}C_J$$
$$C_{L-s}=\frac{4j}{n\pi d}\left(1+\left(\frac{k_n}{k_m}\right)^2\right)\cdot\left(C_{L-s,1}+C_{L-s,2}+C_{L-s,3}\right) \quad (9)$$
$$C_{L-s,1}=\frac{C_{1,s_2}}{\gamma}\cdot\left(\exp\left(\gamma\cdot\left(h_c+g_m\right)\right)-\exp\left(\gamma\cdot g_m\right)\right)$$
$$C_{L-s,2}=-\frac{C_{2,s_2}}{\gamma}\cdot\left(\exp\left(-\gamma\cdot\left(h_c+g_m\right)\right)-\exp\left(-\gamma\cdot g_m\right)\right)$$
$$C_{L-s,3}=\frac{\mu_0\cdot J_p^{m,n}}{\gamma^2}\cdot h_c$$

where $\Psi_{e\text{-}s}$ is the flux linkage. Line integration (dl) of A_{s_2} (magnetic vector potential in the excitation coil region in (5)) in (9) is applied to the excitation coil in the current flow direction, which is shown with the dashed line in Fig. 5. The surface integration (ds) in (9), is for the coil cross-section area, which is averaged over the coil cross-section area, $h_c{\cdot}t_c$. It is shown with a shaded cross section in Fig. 5.

Table II shows the excitation coil inductance calculations using (9) in comparison with the experimental result.

TABLE II
EXCITATION COIL INDUCTANCE WITHOUT MOVING PART

Frequency	Experimental	Analytical
-	3.49 mH	3.34mH

B. *Including Conductive Moving Part*

The partial differential equations, including the moving part regions, are as follows [32], [38]-[39]:

$$\frac{\partial^2 A_{z,r_1}}{\partial x^2}+\frac{\partial^2 A_{z,r_1}}{\partial y^2}+\frac{\partial^2 A_{z,r_1}}{\partial z^2}=0$$
$$\frac{\partial^2 A_{z,r_2}}{\partial x^2}+\frac{\partial^2 A_{z,r_2}}{\partial y^2}+\frac{\partial^2 A_{z,r_2}}{\partial z^2} \quad (10)$$
$$-\mu_0\mu_r\sigma\left(\frac{\partial A_{z,r_2}}{\partial t}+V\cdot\frac{\partial A_{z,r_2}}{\partial x}\right)=0$$
$$\frac{\partial^2 A_{z,r_3}}{\partial x^2}+\frac{\partial^2 A_{z,r_3}}{\partial y^2}+\frac{\partial^2 A_{z,r_3}}{\partial z^2}=0$$

Regions r_1, r_2 and r_3 are addressed to the parts in Fig. 2, which are below the moving part, the moving part and above the moving part, respectively. μ_r is the relative magnetic permeability, σ is the electrical conductivity. Only linear magnetic permeability is considered for iron moving part, due to the low magnetic fields in the eddy current speed sensor, so that the magnetic nonlinearity and hysteresis effects are negligible. V is moving part speed in (10).

The solutions of (10) are presented for regions, r_1, r_2 and r_3 in (11) using Coulomb gauge condition in (2). The constants of (11) are calculated using the boundary conditions [36] in (12), which are presented in (13).

$$A_{z,r_1}^{m,n}=\left(C_{1,r_1}e^{\gamma\cdot y}+C_{2,r_1}e^{-\gamma\cdot y}\right)\cdot e^{j(\omega t-k_m x-k_n z)}$$
$$A_{x,r_1}=-\frac{k_n}{k_m}A_{z,r_1}$$
$$A_{z,r_2}^{m,n}=\left(C_{1,r_2}e^{\lambda\cdot y}+C_{2,r_2}e^{-\lambda\cdot y}\right)\cdot e^{j(\omega t-k_m x-k_n z)} \quad (11)$$
$$\lambda=\sqrt{\gamma^2+j\mu_0\mu_r\sigma(\omega-k_m\cdot V)},\ A_{x,r_2}=-\frac{k_n}{k_m}A_{z,r_2}$$
$$A_{z,r_3}^{m,n}=\left(C_{1,r_3}e^{\gamma\cdot y}+C_{2,r_3}e^{-\gamma\cdot y}\right)\cdot e^{j(\omega t-k_m x-k_n z)}$$
$$A_{x,r_3}=-\frac{k_n}{k_m}A_{z,r_3}$$
$$A_{z,r_1}\left(y=-\infty\right)=0$$
$$H_{x,z,r_1}\left(y=-d\right)=H_{x,z,r_2}\left(y=-d\right)$$
$$B_{y,r_1}\left(y=-d\right)=B_{y,r_2}\left(y=-d\right) \quad (12)$$
$$H_{x,z,r_2}\left(y=0\right)=H_{x,z,r_3}\left(y=0\right)+H_{x,z,s_1}\left(y=0\right)$$
$$B_{y,r_2}\left(y=0\right)=B_{y,r_3}\left(y=0\right)+B_{y,s_1}\left(y=0\right)$$
$$A_{z,r_3}\left(y=\infty\right)=0$$
$$K=\frac{\lambda+\mu_r\cdot\gamma}{\lambda-\mu_r\cdot\gamma}e^{2\lambda\cdot d},\ K'=\lambda\frac{K-1}{K+1}$$
$$C_{2,r_3}=\frac{\mu_r\cdot\gamma-K'}{\mu_r\cdot\gamma+K'}C_{1,s_1},\ C_{1,r_3}=0 \quad (13)$$
$$C_{1,r_2}=\frac{2\mu_r\cdot\gamma}{\mu_r\cdot\gamma+K'}\frac{K\cdot C_{1,s_1}}{1+K},\ C_{2,r_2}=\frac{2\mu_r\cdot\gamma}{\mu_r\cdot\gamma+K'}\frac{C_{1,s_1}}{1+K}$$
$$C_{1,r_1}=\left(C_{1,r_2}\cdot e^{-\lambda\cdot d}+C_{1,r_2}\cdot e^{\lambda\cdot d}\right)\cdot e^{\gamma\cdot d},\ C_{2,r_1}=0$$

The self-inductance of the excitation coil related only to the reaction fields of the induced eddy current in the moving part, $L_{e\text{-}r}$ and the total self-inductance, L_e, are presented in (14). The same procedure as (9) for integration is performed. A_{r_3} is the magnetic vector potential in region r_3.

$$L_e=L_{e-s}+L_{e-r}$$
$$L_{e-r}=\frac{\Psi_{e-r}}{I}=\frac{N_e\int\int A_{r_3}\cdot dlds}{h\cdot t\cdot I}= \quad (14)$$
$$\frac{N_e\cdot L\cdot l}{h\cdot t\cdot I}\sum_n\sum_m C_{L-r}C_J$$
$$C_{L-r}=\frac{4j}{n\pi d}\left(1+\left(\frac{k_n}{k_m}\right)^2\right)\cdot C_{L-r,2}$$
$$C_{L-r,2}=-\frac{C_{2,r_3}}{\gamma}\cdot\left(\exp\left(-\gamma\cdot\left(h_c+g_m\right)\right)-\exp\left(-\gamma\cdot g_m\right)\right)$$

The excitation coil and the pickup coil have the same dimensions and the same number of turns in this paper. The induced voltage in the pick up coil, U_p, can be calculated using (15), which is presented in (16). Only the reaction fields caused by the induced eddy current in the moving part are considered for voltage calculation, as the source fields of the excitation coil do not induce voltage in the pick-up coil.

A final version of this paper was published in
IEEE Trans. Vehicular Technology 70 (2021), pp. 3197-3207, DOI 10.1109/TVT.2021.3065924

$$\Psi_p = \frac{N_p \int\int A_{r_3} \cdot dlds}{h \cdot t} = \frac{N_p \int\int A_{z,r_3} \cdot dzds}{h_c \cdot t_c}, \qquad (15)$$

$$U_p = -\frac{\partial \Psi_p}{\partial t} = -j\omega\Psi_p$$

where Ψ_p is the total average mutual flux linkage over the volume of the pick-up coil. Line integration of A_{r_3} is applied to the pick-up coil region in the artificial current flow direction (the *y*-*z* plane), which is shown with the dashed line in Fig. 4. The line integral is considered only in the *z*-direction of the coil sides, as the *y*-component of the magnetic vector potential is zero. The surface integration in (15) is for the pick-up coil cross-section area shown with a shaded cross section in Fig. 4, which is averaged over the coil cross-section area, $h_c \cdot t_c$. The polarity of the induced voltage changes with the changes in speed direction.

$$U_p = j\omega N_p \sum_m \sum_n C_p^{m,n}$$

$$C_p^{m,n} = 4\frac{j}{k_m k_n} \sin\left(k_m \frac{h_c}{2}\right) \cdot C_{2,r_3} \cdot C_{U-r} \cdot e^{-\gamma \cdot h_p}$$

$$h_p = g_m + h_c + g_c + t_c + \frac{w_c}{2}$$

$$C_{U-r} = \frac{1}{j\gamma + k_n} C_{U-r,1} - \frac{1}{j\gamma - k_n} C_{U-r,2}$$

$$C_{U-r,1} = \sin\left(j\gamma \frac{w_c + 2t_c}{2} + k_n \frac{w_c + 2t_c}{2}\right)$$

$$-\sin\left(j\gamma \frac{w_c}{2} + k_n \frac{w_c}{2}\right)$$

$$C_{U-r,2} = \sin\left(j\gamma \frac{w_c + 2t_c}{2} - k_n \frac{w_c + 2t_c}{2}\right)$$

$$-\sin\left(j\gamma \frac{w_c}{2} - k_n \frac{w_c}{2}\right) \qquad (16)$$

Fig. 5 - Fig. 8 show the 2D magnetic flux lines distribution in the *y*-*x* plane. The magnetic flux lines distribution is the equipotential contour plot of *z*-component of the magnetic vector potential, A_z in the *x*-*y* plane (z=0), where A_x is zero [30]. And the 2D eddy current distribution in the *z*-*x* plane in the moving part. The eddy current distribution is a contour plot of streamline function, I_y in (17) in *x*-*z* plane [40] on the surface of the moving part (y=0).

$$J = \nabla \times I_y$$

$$J_{x,r_2} = -\sigma\left(\frac{\partial A_{x,r_2}}{\partial t} + V \cdot \frac{\partial A_{x,r_2}}{\partial x}\right), I_y = -\int J_{x,r_2} dz$$

$$J_{z,r_2} = -\sigma\left(\frac{\partial A_{z,r_2}}{\partial t} + V \cdot \frac{\partial A_{z,r_2}}{\partial x}\right), I_y = \int J_{z,r_2} dx \qquad (17)$$

$$I_y = \frac{\sigma(\omega - V \cdot k_m)}{k_m} \times$$

$$\sum_n \sum_m \left(C_{1,r_2} + C_{2,r_2}\right) \cdot e^{j(\omega t - k_m x - k_n z)}$$

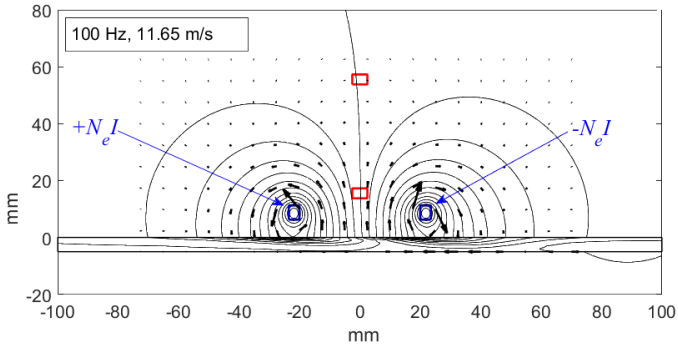

Fig. 5. Magnetic flux distribution and vector plot for an iron moving part in the *y*-*x* plane (z=0)

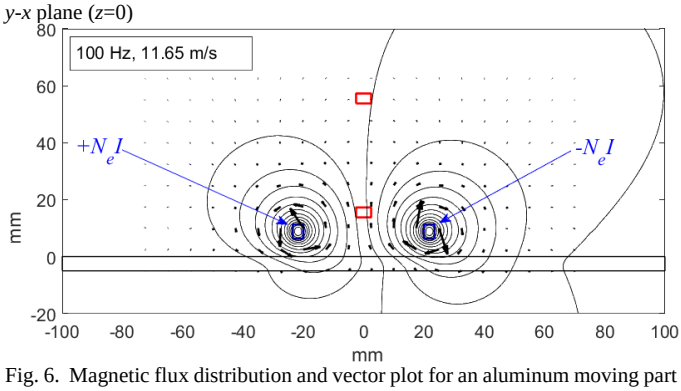

Fig. 6. Magnetic flux distribution and vector plot for an aluminum moving part in the *y*-*x* plane (z=0)

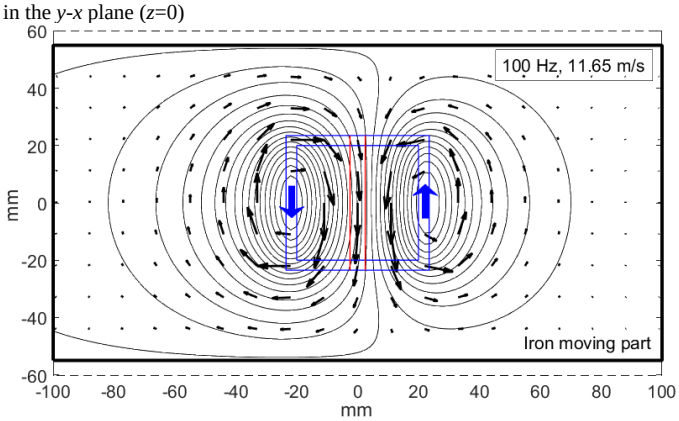

Fig. 7. Eddy current distribution and vector plot on surface of an iron moving part the *z*-*x* plane (y=0) at 100 Hz and 11.65 m/s

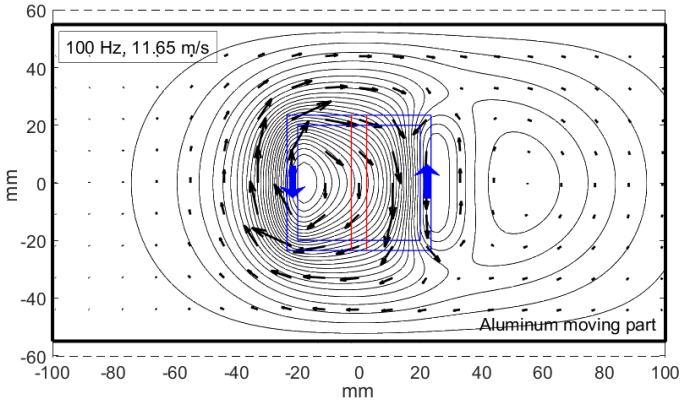

Fig. 8. Eddy current distribution and vector plot on the surface of an aluminum moving part the *z*-*x* plane (y=0) at 100 Hz and 11.65 m/s

Table III shows the analytical and experimental results for self inductance of the excitation coil with an iron moving part at different frequencies. It shows that the analytical modeling is

A final version of this paper was published in
IEEE Trans. Vehicular Technology 70 (2021), pp. 3197-3207, DOI 10.1109/TVT.2021.3065924

highly accurate.

TABLE III
EXCITATION COIL INDUCTANCE WITH AN IRON MOVING PART

Frequency	Experimental	Analytical
20 Hz	4.19 mH	4.02 mH
60 Hz	4.13 mH	3.98 mH
120 Hz	4.09 mH	3.93 mH
240 Hz	4.03 mH	3.87 mH
360 Hz	4.0 mH	3.83 mH
1800 Hz	3.78 mH	3.60 mH
4500 Hz	3.59 mH	3.43 mH

III. EXPERIMENTAL RESULTS

Fig. 9 shows the experimental setup and the eddy current speed sensor. A rotating disk is used to model the linear speed for the sensor. The size of the sensor is very small in comparison with the radius of the rotating disk. The use of a disk or a cylinder is a common method for approximate modeling of linear motion [41]. A lock-in amplifier, SR830 manufactured by Stanford Research Systems is used to measure the pick-up coil voltage. The schematic model of lock-in amplifier is depicted in Fig. 10. The excitation coil with 19 Ω resistance is in series with an external resistance and signal generator as a voltage source with internal resistance 50 Ω and 10 V amplitude. The voltage drop on the ~~of~~ external resistor~~ance~~ is used as reference signal for the lock-in amplifier, which represents excitation coil current.

The experimental results for the real component (U_r) and the imaginary component (U_i) of the pick-up coil voltage are presented in Fig. 11 and Fig. 12 for aluminum and iron moving parts.

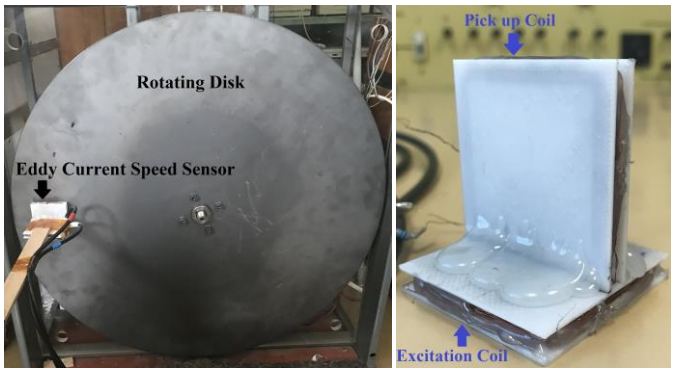

Fig. 9. Experimental set up – A rotating disk as the moving part (left), and the eddy current speed sensor including the excitation coil and the pick-up coil with a perpendicular configuration (right)

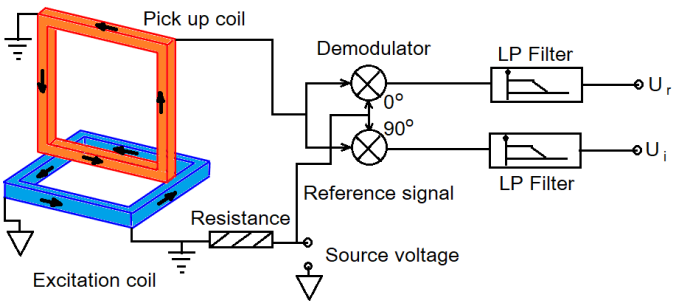

Fig. 10. Schematic model of lock in amplifier and excitation coil and pick up coil

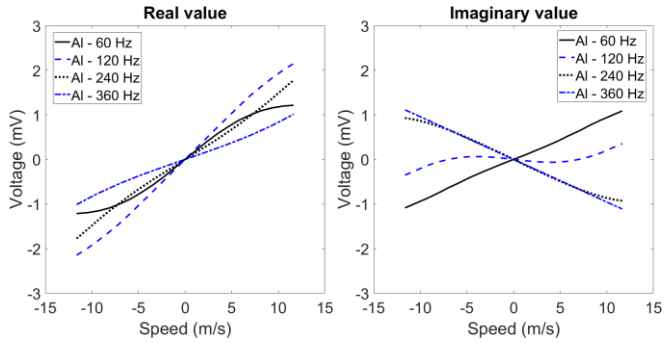

Fig. 11. Experimental results for the real and imaginary components of the pick-up coil voltage (rms value) – Aluminum moving part

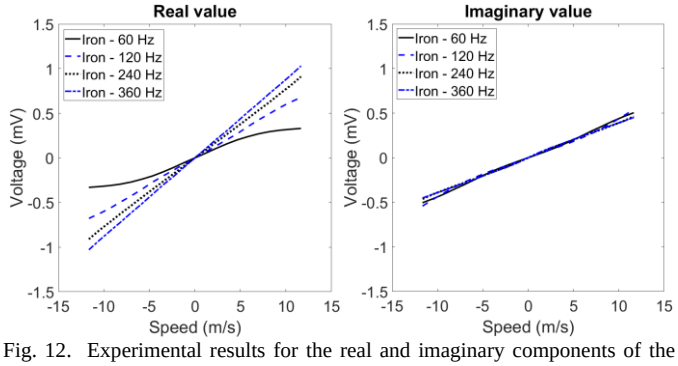

Fig. 12. Experimental results for the real and imaginary components of the pick-up coil voltage (rms value) – Iron moving part

The imaginary and real components of the voltages are obtained relative to the excitation coil current as a reference signal. The pick-up coil-induced voltages show different trends, depending on the materials of the moving part and the excitation frequency. The sensitivity of the sensor is defined for the slope, K of curve fitted ~~straight line~~ linear function of induced voltage, U versus speed, V ~~curve~~ ($U=K\cdot V$). The sensitivity of the speed sensor is higher with an aluminum moving part at lower frequency, but its sensitivity decreases with increasing frequency. The opposite phenomenon occurred in speed sensor performance with an iron moving part, where the sensitivity increases with increasing frequency. The sensitivities for the absolute value of the voltage are 0.08664 mV/(m/s) and 0.09659 mV/(m/s) for an iron moving part at 240 Hz and at 360 Hz, respectively.

The linearity error decreases with an iron moving part at higher frequencies, as shown in Fig. 13 and Fig. 14, which compare the linearity error of real, imaginary and absolute ($U_a = \sqrt{U_r^2 + U_i^2}$) components of the voltage at 240 Hz and at 360 Hz. The error is less than 0.47% for the real component of the voltage at 360 Hz. The distance from the middle of the speed sensor to the outer circumference of the disk is 55 mm, so the parameter L moving part width is physically considered to be 110 mm for analytical modeling (Fig. 3 and Table I). However, parameter L is practically increased to 150 mm in the analytical modeling to take accurately into account the flux leakage around the excitation coil. The comparisons between analytical modeling and the experimental results are shown for aluminum and iron moving parts in Fig. 15 for the absolute component of the voltage, which shows that the analytical model is highly accurate. The analytical calculations fit the ~~coincide well with~~

A final version of this paper was published in
IEEE Trans. Vehicular Technology 70 (2021), pp. 3197-3207, DOI 10.1109/TVT.2021.3065924

measurements with low errors, for example, the error is about 4% and less for iron moving part at 360 Hz (Fig. 16). Therefore, the analytical model is a suitable computational tool for parametric analysis and design optimization of sensor and its performance analysis at higher speeds.

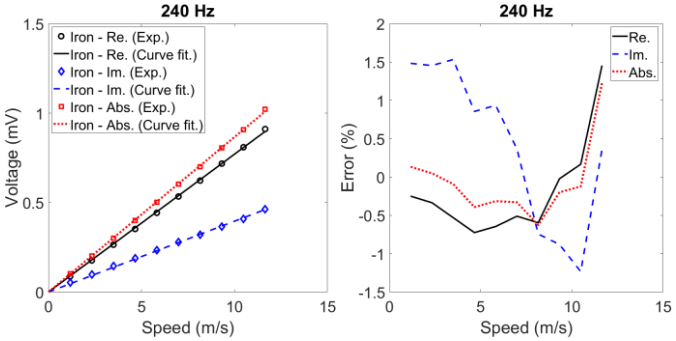

Fig. 13. Experimental voltages and linear curve fitting and linearity error results for the real (Re), imaginary (Im) and absolute components of the pick-up coil voltage at 240 Hz

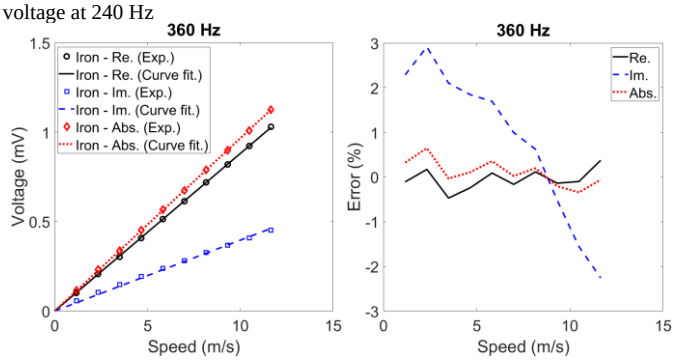

Fig. 14. Experimental voltages and linear curve fitting and linearity error results for the real (Re), imaginary (Im) and absolute (Abs) components of the pick-up coil voltage at 360 Hz

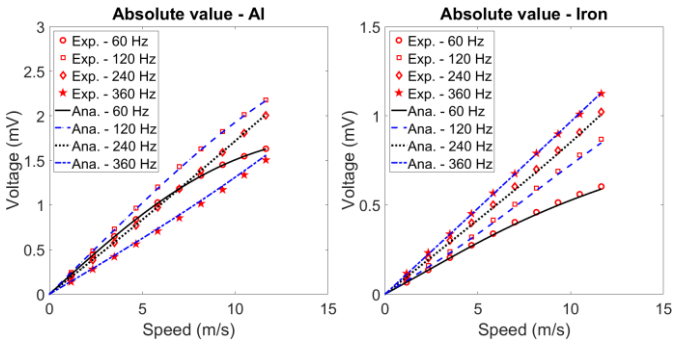

Fig. 15. A comparison between the experimental and analytical results for the absolute component of the pick-up coil voltage

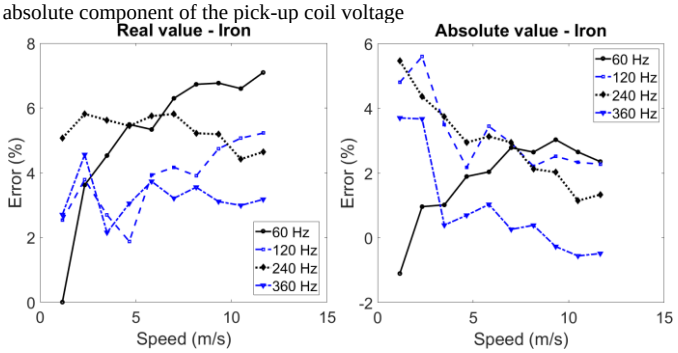

Fig. 16. Error comparison between analytical and measurements results for iron moving part of Fig. 15

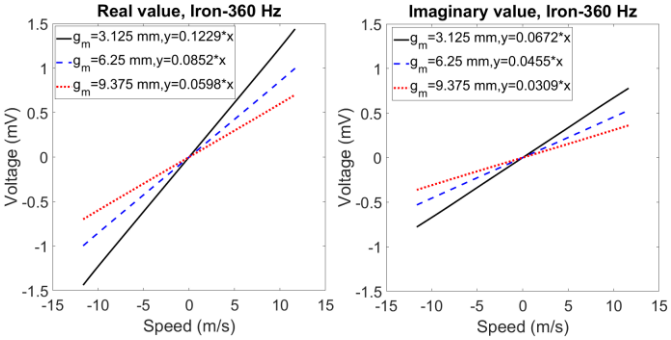

Fig. 17. The real and imaginary component of the pick-up coil voltage for different mechanical airgaps at 360 Hz – Analytical

IV. Parametric Analysis for An Iron Moving Part

The mechanical or magnetic airgap variation, g_m, is a high influence factor on the eddy current speed sensor performance, as shown in Fig. 17. The sensitivity values are presented in Table IV for different mechanical gaps, g_m. Its effect is stronger on the imaginary component of the voltage when sensitivities are compared at different mechanical gaps. This is the case when the iron moving part is not perfectly smooth, voltage versus speed curve can be less linear.

TABLE IV
Sensitivity Factors Concerning Fig. 17

Gap, g_m	Real, K_R	Imaginary, K_I
3.125 mm	0.1229 mV/m/s	0.0672 mV/m/s
6.25 mm	0.0852 mV/m/s	0.0455 mV/m/s
9.375 mm	0.0598 mV/m/s	0.0309 mV/m/s

Solid irons and steels used in construction have different conductivities and initial relative magnetic permeabilities, which depend on their chemical composition and on the manufacturing process, as has been shown for solid irons used in railway construction [42]-[43]. The conductivity and the magnetic permeability of solid iron are highly dependent on temperature [44]. For example, the measured conductivity and the temperature, θ (°C),-dependency of the used solid iron moving part in this paper is: σ (MS/m)=6.2/(1+0.0045·(θ-20)). For instance, the conductivities of iron, σ (MS/m) are 7.6, 6.8, 6, 5.7 at -20 °C, 0 °C, 27 °C, and 40 °C, respectively. Therefore, temperature compensation is required for industrial applications of the eddy current speed sensor.

Fig. 18 shows the pick-up coil voltage versus speed for various values of conductivity and relative permeability of an iron moving part. The pick-up coil voltage increases with decreasing relative permeability and increasing conductivity. It is noticeable from the voltage values at 360 Hz excitation frequency that the higher conductivity and lower permeability of solid iron cause higher sensitivity for the eddy current speed sensor. The sensitivity increases by 37% with decreasing relative permeability from 125 to 50 for σ = 4.0 MS/m and it increases by 30% for σ = 7.0 MS/m. The sensitivity decreases by 13% with decreasing conductivity from 7.0 MS/m to 4.0 MS/m for μ_r = 50, and it decreases by 18% for μ_r = 125. The sensitivity values are presented in Table V concerning Fig. 18.

TABLE V

A final version of this paper was published in
IEEE Trans. Vehicular Technology 70 (2021), pp. 3197-3207, DOI 10.1109/TVT.2021.3065924

SENSITIVITY FACTORS CONCERNING FIG. 18

Cond.	Abs, K_A, mV/m/s μ_r= 50	Abs, K_A, mV/m/s μ_r= 75	Abs, K_A, mV/m/s μ_r= 100	Abs, K_A, mV/m/s μ_r= 125
4 MS/m	0.1063	0.0915	0.0835	0.0775
5 MS/m	0.1114	0.0991	0.0908	0.0842
6 MS/m	0.1172	0.1054	0.0966	0.0897
7 MS/m	0.1226	0.1107	0.1015	0.0944

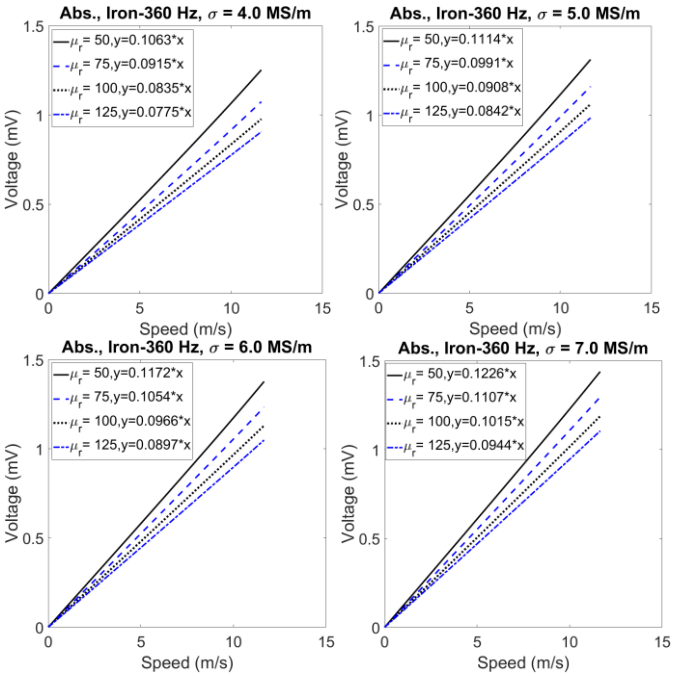

Fig. 18. The absolute (Abs) component of the pick-up coil voltage with different conductivity and relative permeability for an iron material – Analytical

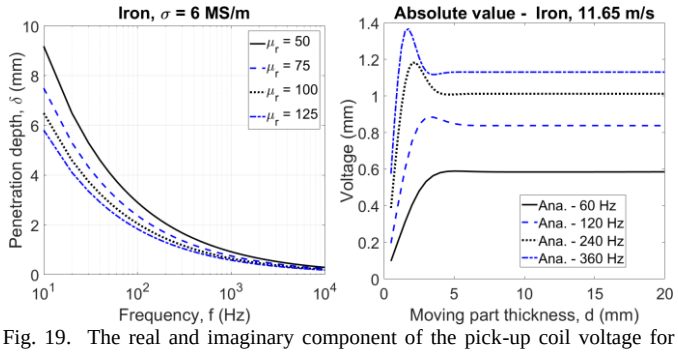

Fig. 19. The real and imaginary component of the pick-up coil voltage for different mechanical airgaps at 360 Hz – Analytical

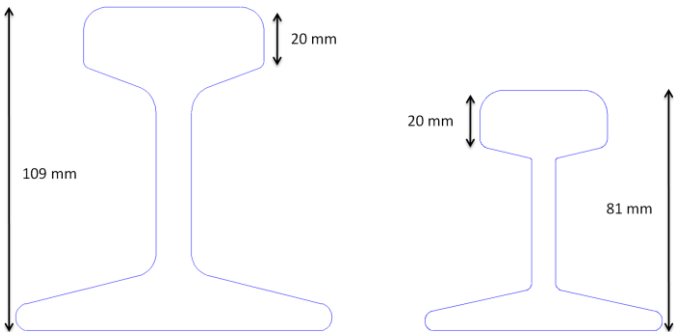

Fig. 20. Railhead dimensions for typical rails [41]

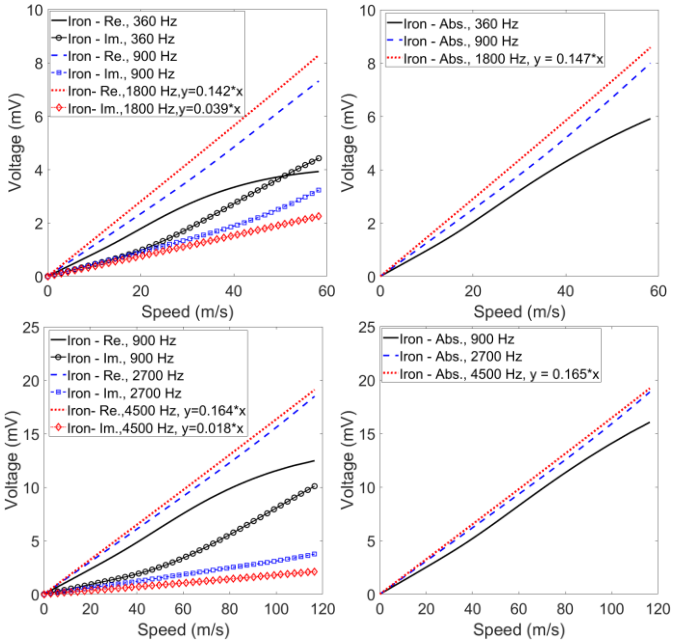

Fig. 21. The real, imaginary and absolute component of the pick-up coil voltage at higher speeds – Analytical

The skin and magnetic flux penetration depth ($\delta = 1/\sqrt{\pi f \sigma \mu_r \mu_0}$) versus frequency up to 10 kHz and the induced voltage of the eddy current speed sensor versus moving iron part thickness up to 20 mm are shown in Fig. 19. It is shown that skin effect in the proposed eddy current sensor is negligible if a practical application is in railways, as ~~which~~ the railhead height is about 20 mm according to Fig. 20 [45].

V. ANALYSIS OF HIGHER SPEEDS

The voltage results of an eddy current speed sensor at higher speeds of about 58 m/s (210 km/h) and 117 m/s (420 km/h) are presented in Fig. 16. Excitation frequencies of 1.8 kHz and 4.5 kHz are quite sufficient for maximum speeds of 58 m/s and 117 m/s in order to obtain satisfactory linearity for the speed sensor in the whole speed range. The excitation current amplitude, I = 135 mA, (Table I) is used for the analysis of the eddy current sensor and induced voltage calculations in Fig. 21 at higher frequencies.

However, the reactance of the excitation coil could have influence~~be influential~~ on the excitation current amplitude at high frequencies with a constant voltage source of the excitation coil. For example, the reactances (ωL_e) of the excitation coil are calculated as 9.05 Ω, 42.75 Ω and 101.51 Ω using the inductance values in Table III at 360 Hz, 1.8 kHz and 4.5 kHz, respectively. Equation (18) presents excitation current amplitude, I function of source voltage amplitude, U_s , source internal resistance, R_s, external resistance~~,~~ R_{ex}, excitation coil resistance, R_e and excitation coil reactance, ωL_e. For example, the current amplitudes, I were~~are~~ calculated 0.137 A, 0.119 A and 0.080 A (in this paper, R_s=50 Ω, R_{ex}=3.7 Ω, =19 Ω) without consideration of cable impedance at frequencies, 360 Hz, 1.8 kHz and 4.5 kHz, respectively.

A final version of this paper was published in
IEEE Trans. Vehicular Technology 70 (2021), pp. 3197-3207, DOI 10.1109/TVT.2021.3065924

$$I = \frac{U_s}{\sqrt{\left(R_s + R_{ex} + R_e\right)^2 + \left(\omega L_e\right)^2}} \quad (18)$$

A higher source voltage is therefore required to keep the excitation current amplitude large enough to obtain sufficient sensitivity for the sensor at higher frequencies.

TABLE VI
SENSITIVITY FACTORS CONCERNING FIG. 21

Frequency	Re, K_R, mV/m/s	Im, K_I, mV/m/s	Abs, K_A, mV/m/s
1800 Hz	0.142	0.039	0.147
4500 Hz	0.164	0.018	0.165

VI. DISCUSSIONS

The wire diameter of the excitation coil in this paper is 0.2 mm and the current density in the wire is 3.03 A/mm^2, which does not heat up the excitation coil even without forced cooling. The skin effect is calculated less than 0.1% on the winding losses at 4.5 kHz. Induced eddy current losses in the moving part iron caused by excitation coil is negligible as ampere turn of excitation coil is only 26.9 AT (Ampere turn - amplitude) and the sensor has air coil configuration with 6.25 mm magnetic gap between the coil and moving part, therefore surface heating of moving part is negligible even with a larger current in large size of disk shape moving part in this paper or real iron rails in comparison with the sensor dimensions. Temperature compensation in the eddy current speed sensor is required against heating of excitation coil and moving part or iron rails.

The main advantages of perpendicular type of eddy current speed sensor in comparison with parallel type one with magnetic shielding and yoke in [31] are: 1- it has single pick up coil and less asymmetrical position error relative to the excitation coil in comparison with two pick up coils in parallel type. 2- It is more suitable at high speeds as reactance of excitation coil is less in air coil eddy current sensor and the excitation coil current becomes less dependent on the temperature. 3- The variations of magnetic properties of the magnetic yoke in [31] due to the ageing or operation in a harsh environment, for example, railways could affect sensor performance, which is avoided in air coil perpendicular speed sensor despite its less sensitivity.

The proposed speed sensor has merits for industrial applications, for example, for railways over traditional methods for speed measurements using variable reluctance wheel with Hall sensor and alternative optical one [46], which are simple and cost effective structure, lower maintenance, higher mechanical sensor fault tolerant, direct measurement of linear speed avoiding wheel sliding and slipping error, and nondestructive methodology ~~and etc~~.

Industrial designs of noncontacting inductive proximity and inductive linear displacement sensors with a miniaturized configuration for magnetic and electronic signal processing and conditioning parts were presented in [47]-[48]. They used 2D and 3D finite element method for analysis and simple analytical calculations for the sensors evaluations. Their methodologies could be utilized for liftoff compensation of eddy current speed sensor and miniaturization of electronic for industrial models.

VII. CONCLUSION

Experimental and theoretical results for a perpendicular-type eddy current speed sensor with air coils have been presented. Solid iron moving parts and aluminum moving parts were both considered for an evaluation of the material effects on the eddy current speed sensor. Different excitation frequencies were utilized in order to obtain greater linearity and sensitivity, especially with the solid iron moving part. Increasing frequency improves the linearity of the eddy current speed sensor with a solid iron moving part. The linearity error for a solid iron moving part could be as low as 0.5% at 360 Hz excitation frequency, which makes the proposed speed sensor a suitable potential option for linear speed measurements. Lower relative permeability and higher conductivity cause higher sensitivity of the sensor. The power consumption of the eddy current speed sensor is 173 mW with excitation coil resistance of 19 Ω.

A performance evaluation of the eddy speed sensor at high speed, 117 m/s (420 km/h) has also been presented. It shows excellent linearity of 0.43% at 4.5 kHz excitation frequency.

Optimization of a perpendicular-type eddy current speed sensor in terms of maximizing its sensitivity to the power consumption ratio is planned for future work. Compensation of the mechanical gap variation and the temperature dependency effects of moving part materials will also be investigated in the future.

ACKNOWLEDGMENT

The authors thank Mr. A. Chirtsov and Dr. J. Vyhnanek, from the Department of Measurement for the measurements. This work was supported by the Czech Technical University within the framework of Grant SGS18/187/OHK3/3T/1.

REFERENCES

[1] R. J. Hill, "Fail-safe speed sensor for London Transport automatic trains," *IEE Proc.*, vol. 128, no. 6, pp. 277-284, Nov. 1981
[2] Y. Hikasa, and Y. Takeuchi, "Detail and experimental results of ferromagnetic levitation system of Japan air Lines HSST-01/-02 Vehicles," *IEEE Trans. on Vehicular Technology*, vol. 29, no. 1, pp. 35-41, Feb. 1980
[3] R. G. Rule, and R. G. Gilliland, "Combined magnetic levitation and propulsion: the Mag-Transit concept," *IEEE Trans. on Vehicular Technology*, vol. 29, no. 1, pp. 41-49, Feb. 1980
[4] P. Liljas, "Speed and positioning systems. The traditional way," *IEE Colloquium on Where Are We Going?* pp. 2/1-2/9, 1997
[5] J. Lu, M. Wu, G. Liu, X. Geng, "Research on fault diagnosis method for speed sensor of high-speed train," *2019 Prognostics and System Health Management Conference (PHM-Qingdao)*, Oct. 2019
[6] X.Hu, T. Chen, N. Zhao, "Simulation analysis of train speed measurement technology based on urban rail transit system," *2016 International Conference on Intelligent Transportation, Big Data & Smart City (ICITBS)*, pp. 186-192, Dec. 2016
[7] P. Deng, C. Dai, Z. Long, "Optimum design and implementation of signal processing method for position and speed measurement system of high-speed maglev train," *2019 Chinese Automation Congress (CAC)*, pp. 186-192, Nov. 2019
[8] L. Du, Q. Sun, J. Bai, X. Wang, T. Xu, "Speed calibration and traceability for train-borne 24 GHz continuous-wave Doppler radar sensor," *Sensors*, vol. 20, 1230, 2020
[9] J. Rickman, "Eddy current turbocharger blade speed detection," *IEEE Trans. Magn.*, vol. MAG-18, no. 5, pp. 1014–1021, Sep. 1982

A final version of this paper was published in
IEEE Trans. Vehicular Technology 70 (2021), pp. 3197-3207, DOI 10.1109/TVT.2021.3065924

[10] J. O. Manyala, T. Fritz, and M. Z. Atashbar, "Gearbox speed sensor design and performance optimization," *IEEE Sensors J.*, vol. 13, no. 2, pp. 629-636, February 2013

[11] T. Addabbo, M. Di Marco, A. Fort, E. Landi, M. Mugnaini, V. Vignoli, and G. Ferretti, "Instantaneous rotation speed measurement system based on variable reluctance sensors for torsional vibration monitoring," *IEEE Trans. Instrum. Meas.*, vol. 68, no. 7, pp. 2363-2373, July 2019

[12] J. Guzinski, H. Abu-Rub, M. Diguet, Z. Krzeminski, and A. Lewicki, "Speed and load torque observer application in high-speed train electric drive," *IEEE Trans. on Industrial Electronics*, vol. 57, no. 2, pp. 565-574, Feb. 2010

[13] R. Dian, W. Xu, J. Zhu, D. Hu, and Y. Liu, "An improved speed sensorless control strategy for linear induction machines based on extended state observer for linear metro drives," IEEE *Trans. on Vehicular Technology*, vol. 67, no. 10, Oct. 2018

[14] H. Wang, X. Ge, Y. Yue, and Y.-C. Liu, "Dual phase-locked loop-based speed estimation scheme for sensorless vector control of linear induction motor drives," *IEEE Trans. on Industrial Electronics*, vol. 67, no. 7, pp. 5900-5912, July 2020

[15] J.J. Stickler, "Comparison of theories for high-speed linear induction motors," *IEEE Trans. on Vehicular Technology*, vol. 29, no. 1, pp. 65-71, February 1980

[16] S. Nonaka and T. Higuchi, "Design of single-sided linear induction motors for urban transit," *IEEE Trans. on Vehicular Technology*, vol. 37, no. 3, pp. 167-173, August 1988

[17] D. Valderas , I. Mesa, I. Adin, H. Lehmann , G. Lancaster, O. Stark, W. Baldauf, and J. del Portillo, "Modeling eddy current brake emissions for electromagnetic compatibility with signaling devices in high-speed railways," *IEEE Trans. on Vehicular Technology*, vol. 66, no. 11, pp. 9743-9752, November 2017

[18] J. A. Shercliff, *The Theory of Electromagnetic Flow Measurement*, Cambridge University Press, 1962.

[19] P. Ripka, *Magnetic Sensors and Magnetometers*, Artech House, Jan. 1,2001

[20] T. J. Rocha, H. G. Ramos, A. L. Ribeiro, and D. J. Pasadas, "Evaluation of subsurface defects using diffusion of motion-induced eddy currents," *IEEE Trans. Instrum. Meas*., vol. 65, no. 5, pp. 1182–1187, May 2016

[21] T. Itaya, K. Ishida, A. Tanaka, N. Takehira, and T. Miki, "Analysis of a fork-shaped rectangular coil oriented perpendicular to moving conductor slabs," *NDT&E International*, 44, 413–420, 2011

[22] J. Wu, J. Zhu, G. Tian, H. Xia, X. Huang, and C. Tang, "Study of rotating magnet array-based motion-induced eddy current thermography," *IEEE Trans. on Magnetics*, vol. 54 , no. 12, 6203105, Dec. 2018

[23] Y.S. Sun, W. Lord, G. Katragadda, and Y.K. Shin, "Motion induced remote field eddy current effect in a magnetostatic non-destructive testing tool: a finite element prediction," *IEEE Trans. on Magnetics*, vol. 30 , no. 5, pp. 3304-3307, Sept. 1994

[24] E. Cardelli, A. Faba, and F. Tissi, "Contact-less speed probe based on eddy currents," *IEEE Trans. Magn.*, vol. 49, no. 7, pp. 3897–3900, Jul. 2013

[25] T. Sonoda, R. Ueda, K. Fujitani, T. Irisa, and S. Tatata, "DC magnetic field type eddy current speed sensor detecting cross magnetization field with amorphous core," *IEEE Trans. Magn.*, vol. MAG-21, no. 5, pp. 1732–1734, Sep. 1985

[26] C. Gong, A. Tuysuz, M. Flankl, T. Stolz, J. Kolar, T. Habetler, "Experimental analysis and optimization of a contactless eddy-current-based speed sensor for smooth conductive surfaces," *IEEE Trans. on Industrial Electronics*, 67(10), pp. 8817 - 8828, October 2020

[27] N. Takehira, and A. Tanaka, "Analysis of a perpendicular-type eddy-current speed meter," *IEE Proc. A – Phys. Science, Meas. and Instr., Manag. and Educ.- Rev.* , vol. 135 ,no. 2, pp. 89 - 94, Feb. 1988

[28] T. Itaya, K. Ishida, A. Tanaka, and N. Takehira, "Analysis of an eddy current speed meter by rectangular coil system," *IEEJ Trans. on Fund. and Mat.* 133(8), pp. 416-423 , January 2013

[29] M. Mirzaei, P. Ripka, A. Chirtsov, and J. Vyhnanek, "Eddy current linear speed sensor," *IEEE Trans. Mag.*, vol. 55 , no. 1 , pp. 1-4, 2019

[30] M. Mirzaei, P. Ripka, A. Chirtsov, J. Vyhnanek, and V. Grim, "Design and modeling of a linear speed sensor with a flat type structure and air coils," *J. of Magnetism and Magnetic Materials*, vol. 495, 165834, 2020

[31] M. Mirzaei, P. Ripka, A. Chirtsov, and V. Grim, "Eddy current speed sensor with magnetic shielding," *J. of Magnetism and Magnetic Materials*, vol. 502, 166568, May 2020

[32] K. Yoshida, "New transfer-matrix theory of linear induction machines, taking into account longitudinal and transverse ferromagnetic end effects," *IEE Proceedings B – Elect. Power Appl*., vol. 128 , no. 5, pp. 225-236, Sept. 1981

[33] Y. Marechal, G. Meunier, Computation of 2D and 3D eddy currents in moving conductors of electromagnetic retarders, IEEE Trans. Mag., vol. 26, no. 5, pp. 2382-2384, Sept. 1990

[34] T. Morisue, "A Comparisn of the Coulomb gauge and Lorentz gauge magnetic vector potential formulations for 3D eddy current calculations," *IEEE Trans. Mag.*, vol. 29, no. 2, pp. 1372-1375, March 1993

[35] T.Onuki, S.Wakao, and T.Yamamura, "Physical meaning of gauge conditions in eddy current analysis," *IEEE Trans. Mag.*, vol. 29, no. 6, pp. 2452-2454, Nov. 1993

[36] K.J. Binns, P.J. Lawrenson, and C.W. Trowbridge, *The Analytical and Numerical Solutions of Electric and Magnetic Fields*, Published by John Wiley & Sons Ltd., 1992

[37] M. N. O. Sadiku, *Numerical Techniques in Electromagnetics*, Second Edition, July 12, 2000 by CRC Press, Textbook

[38] S. Yamamura, *Theory of Linear Induction Motors*. Second Edition. John Wiley & Sons, 1979

[39] M. Poloujadoff, *The Theory of Linear Induction Machinery*, Clarendon Press, 1980

[40] D. Schieber, *Electromagnetic Induction Phenomena*, Springer-Verlag, 1986 - Science

[41] O. C. Coho, G.B. Kliman, J. I. Robinson, "Experimental evaluation of a high speed double sided linear induction motor," *IEEE Transactions on Power Apparatus and Systems*, vol. 94, no. 1, pp. 10-18, 1975

[42] R. J. Hill, D. C. Carpenter, "Modeling of nonlinear rail impedance in AC traction power systems," *IEEE Transactions on Power Delivery*, vol. 6, no. 4, pp. 1755 – 1761, 1991

[43] R. Langman, "Measurement of reversible permeability using solid (nonlaminated) specimens," *Proc. 1EE*, vol. 117, no. 9, pp. 1887-1890, September 1970

[44] M. Mirzaei, P. Ripka, A. Chirtsov, and V. Grim, "Temperature stability of the transformer position transducer for pneumatic cylinder," *J. of Magnetism and Magnetic Materials*, vol. 503, 166636, 2020

[45] M. Mirzaei, P. Ripka, "Analysis of material effect on rail impedance,"*53rd International Universities Power Engineering Conference (UPEC)*, UK, 4-7 Sept. 2018

[46] J. Feng, J. Xu, W. Liao and Y. Liu, "Review on the traction system sensor technology of a rail transit train," *Sensors*, vol. 17, 1356, 2017

[47] M. Jagiella, S. Fericean, and A. Dorneich, "Progress and recent realizations of miniaturized inductive proximity sensors for automation," *IEEE Sens. J.*, vol. 6, no. 6, pp. 1734-1741 , Nov. 2006

[48] S. Fericean, and R. Droxler, "New noncontacting inductive analog proximity and inductive linear displacement sensors for industrial Automation," *IEEE Sens. J.*, vol. 7, no. 11, pp. 1538-1545 , Nov. 2007